InterPore
JOURNAL

ACCEPTED ARTICLE

HEAT-ACTIVATED EPOXY FOAM FOR PERMEABILITY ALTERATION IN FRACTURED GEOTHERMAL FIELDS: *PROOF OF CONCEPT*

Dani Or[1,2], Rishi Parashar[3], Ying Yang[4], Manish Bishwokarma[4], Satish Karra[5], Yutong Cui[1]
[1]*Department of Civil and Environmental Engineering, University of Nevada, Reno, NV, USA*
[2]*Department Environmental Systems Science, ETH Zurich, Switzerland*
[3]*Division of Hydrologic Sciences – Desert Research Institute, Reno, NV, USA*
[4]*Department of Chemistry, University of Nevada, Reno, NV, USA*
[5]*Pacific Northwest National Lab, Richland, WA, USA*

Correspondence to:
Yutong Cui,
yutongc@unr.edu

How to Cite:
Or, D., Parashar, R. ., Yang, Y., Bishwokarma, M., Karra, S., Cui, Y. (2026 accepted article). Heat-activated Epoxy Foam for Permeability Alteration in Fractured Geothermal Fields: Proof of Concept. *InterPore Journal*. https://doi.org/10.69631/3mjx5y19

RECEIVED: 4 Jul. 2025
ACCEPTED: 28 Oct. 2025

ABSTRACT

Geothermal energy plays a growing role in the transition to renewable and carbon free energy sources. A challenge for many geothermal operations is how to enhance water-rock heat exchange either by creation of new fractures in a tight rock, or by blocking short-circuiting large conduits. Here we report a novel approach for blocking large aperture (cm scale) fractures using heat-activated epoxy resin foam. The foam is injected as discrete inert resin droplets that are transported to regions of the geothermal field and activated upon reaching sufficiently high temperatures, where they undergo foaming and curing, thereby locally reducing permeability. In contrast to alternative methods for reducing rock permeability such as silicate gels or heat responsive polymer microbeads that target fractures of small apertures (< 0.1), the epoxy foam can reduce permeability of fractures with large apertures (~ 10) while attaining mechanical strength and thermal stability. Results from laboratory aluminum-glass fracture models provide insights by visualizing the transport phase of resin droplets and their subsequent temperature-induced foaming and curing transformations with associated flow pathway blocking. Modeling results for transport and foaming in a simple fracture considering rheological properties and foaming (volume expansion) behavior are compared with measurements of permeability changes. Challenges associated with upscaling to fracture networks and large transport distances of resin droplets are discussed.

KEYWORDS

geothermal energy, epoxy foam, permeability reduction

1. INTRODUCTION

Geothermal resources offer clean, steady and renewable sources of energy for electricity production and heating. In addition to geographical challenges and considerable capital investment into a poorly constrained subsurface, many geothermal fields require fluids (water or brine) to extract heat from the subsurface and sufficient permeability to support high flows required for commercial heat extraction [12, 15]. Among the wide range of heat extraction methods from geothermal fields, we focus here on challenges of conventional geothermal extraction that require drilling to extract natural liquid flows [15], [33], and enhanced geothermal systems (EGS) in which wells are drilled into dry hot rock requiring injection and extraction of heated liquid [12]. Regardless of specific conditions, the lifetime and performance of geothermal fields are defined by the effective fracture area and stimulated rock volume that the circulating fluids can access [25], [27]. However, while a larger accessible fracture area generally enhances geothermal performance, the specific geometry and connectivity of these fractures play a crucial role in determining efficiency [21]. In particular, if the fracture network includes large-aperture faults or highly permeable connections between injection and production wells, it may lead to short-circuiting, where fluids bypass much of the reservoir rock. Short-circuiting reduces the residence time of the working fluid within the reservoir, where injected fluids tend to follow the path of least resistance, often flowing rapidly through high-permeability zones without adequately sweeping the reservoir. This uneven flow distribution not only leads to localized cooling and under-utilization of the stimulated rock volume, but can also accelerate thermal drawdown near the production well.

In geothermal fields containing extensive fault zones or well doublets that are connected by large aperture fractures, heat extraction efficiency may be adversely impacted by such ”short circuiting” flow pathways [6], [8]. The occurrence of short-circuiting is not solely governed by the initial fracture geometry or permeability contrasts but can also be exacerbated by reservoir stimulation processes. Induced seismicity during EGS operation can result in ’hyperpermeable’ pathways, as documented in Rosemanowes Quarry [13, 26] where preferential fluid circulation along these shortcuts results in cooling out and reduces the efficiency of the EGS system. Advances in drilling technology adopted from the petroleum industry are now being incorporated in EGS, for example, the use of closely spaced horizontal well configurations [12] that require stimulation of fractures to hydraulically connect injection and extraction well pairs [15] introducing susceptibility to creation of short-circuiting pathways [12]. This study aims to examine and provide solutions for scenarios in which well doublets become connected by large aperture fractures (natural or stimulated) resulting in reduced heat extraction efficiency. We hypothesize that targeted reduction of permeability in flow-dominating fracture zones can potentially restore idle geothermal wells (at relatively small capital expenditure) and improve thermal performance of production wells experiencing rapid or unsustainable temperature decline.

We report a novel approach for blocking high permeability pathways in fractured geothermal reservoirs using heat-activated foaming epoxy resin [30]. The basic concept is described in Figure 12. Briefly, we seek to inject swarms of resin droplets that are passively carried by the injected liquid and subsequently become thermally activated at target temperatures. A central hypothesis critical for the success of the proposed method is that the injection of uniform (at very low concentration) of resin droplets would be preferentially carried to the highly conductive pathways in proportion to the volumetric flow passing through these conduits. The thermal activation entails release of CO2 blocked resin curing agent at prescribed temperature (presently 120) at which CO2 molecules are released and simultaneously induce foaming and volume expansion as well as spontaneous epoxy resin cross linking and rapid hardening (curing) of the foam. The primary advantages of heat-activated foaming epoxy resin over other measures for permeability reduction, such as silicate gels [10] and temperature-responsive polymers [20], is the high degree of control of the injected resin droplets (size, viscosity), the ability to prescribe activation temperature, and, importantly, the capacity to block large fractures (in the range of 10^{-4} to 10^{-2} m). These characteristics not only enhance placement precision but also allow the injected resin to respond dynamically to evolving subsurface heterogeneity. We anticipate that flow pathways and preferential response

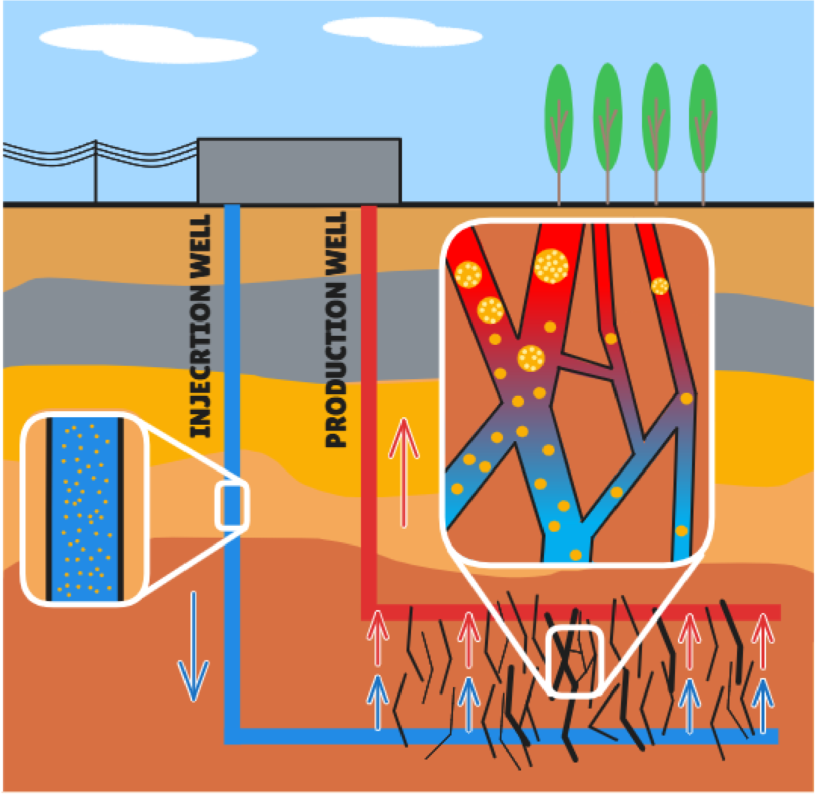

Figure 1: Schematic of an Enhanced Geothermal System (EGS) with injection and production parallel wells and hypothetical behaviour of individual heat-sensitive resin droplets within fractures (showing expansion and foaming in the hot region).

to locally high permeability regions [5, 29] will direct a proportional number of resin droplets into highly conductive fractures. Secondary advantages of this approach over other methods include the insensitivity of resin droplets to carrier fluid properties (e.g., pH is known to affect setting of silicate gels) and the high thermal stability of the cured epoxy foam (up to 280). Epoxy resin has been widely employed as a binding material in rock mass consolidation, chemical grouting, and rammed earth engineering. Due to its good resistance to acid, alkali, and salt corrosion, epoxy resin has also been utilized for the stabilization of contaminated soils [19], wastewater treatment applications [23] and coating materials under high salinity environment [4]. In the long term, the epoxy resin may go through thermal degradation under heat-water environment [3] and lead to gradual failure or blocked pathways. Some certain maintenance regime or constant low concentration of injection should be applied in real field applications.

2. SYNTHESIS AND PROPERTIES OF HEAT ACTIVATED FOAMING EPOXY RESIN AND INJECTION SCENARIOS

The basic requirements for the synthesis of thermally activated epoxy resin are stability during injection, transport, and subsequent expansion (foaming), and curing at a prescribed temperature [30, 31, 22]. For this proof of concept study, we used commercially available epoxy resin, Epon 813, with a viscosity of 0.8. The resin is mixed with CO2 blocked diamine curing agent . The CO2 blocking renders the amine non-reactive under ambient temperature conditions. Release of CO2 aboveat a critical temperature of 125 simultaneously increases the volume of the resin (foaming) and activates amine group that, in turn, initiate the curing process of the epoxy foam via cross-linking of the epoxy base. This foaming and curing process leads to the formation of epoxy foam with substantial volume expansion (tenfold or > 1000% at 125 - see Figure 1). This process is irreversible and lasts only a few minutes (depending on ambient temperature, with higher temperature accelerating reaction rates). The primary reaction of the resin is neither sensitive

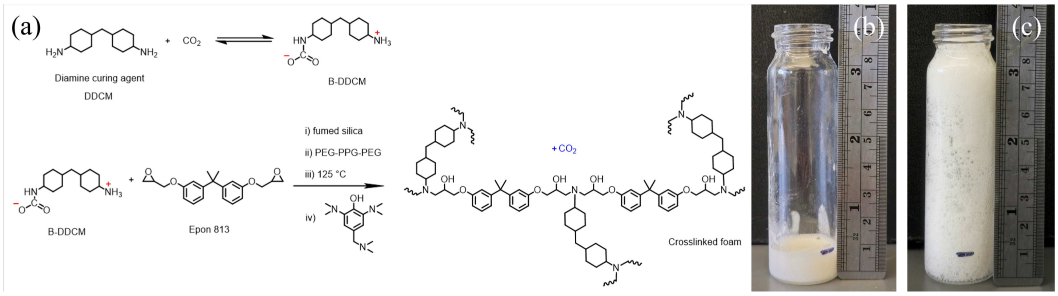

Figure 2: Reaction scheme and resin mixture sample. (a) formation of CO2-blocked amine (B-DDCM) and the reaction to synthesize crosslinked epoxy foam using Epon 813, B-DDCM in the presence of 2,4,6-tris(dimethylaminomethyl)phenol catalyst, fumed silica, and PEG-PPG-PEG at 125; (b) and (c) Resin mixture sample before and after heating to critical temperature (125), foaming and curing.

nor exposed to the environment (pH, salinity, Eh, EC), it is confined within the resin droplet triggered by external temperature. Other critical processes such as foaming and curing are also independent of ambient conditions other than temperature (such resins are used routinely in saline marine systems). The cured resin solidifies forming a cellular structure due to entrappedthe trapped CO2 gas bubbles. The exact resin formulation wasis selected based on target foaming temperature, rapid curing rates, and low resin viscosity to facilitate injection and transport.

Resin synthesis: The CO2-blocked amine curing agent was prepared by dissolving 15 of 4,4-diaminodicyclohexylmethane (DDCM) in 45 dichloromethane (DCM) solvent, followed by bubbling CO2 gas through the solution for 3 hours. The product, CO2-blocked DDCM (B-DDCM), is insoluble in DCM and precipitates out as a white solid. The precipitate was dried in a 50 oven for 12 hours producing a yield of 98%. The resin mixture involving epoxy resin (Epon 813) (2.970, 7.80), B-DDCM (1.000, 3.93), fumed silica (0.020, 0.50 wt.%), poly(ethylene glycol)-block-poly(propylene glycol)-block-poly(ethylene glycol) (PEG-PPG-PEG) (0.058, 1.55 wt.%), and 2,4,6-tris(dimethylaminomethyl)phenol (1.00 wt.%) was mixed mechanically until a homogeneous mixture was obtained. A stoichiometric balance between the amine protons and epoxide group at 1:1 molar ratio was maintained. Ammonium carbamates serve as the CO2-blocked amine crosslinker. They are stable at room temperature, but decompose at elevated temperatures into CO2 as the latent foaming agent and amine as the curing agent. Heating to 125 causes release of CO2, activating the crosslinker which then reacts with epoxy group of Epon 813 resin. The 2,4,6-tris(dimethylaminomethyl)phenol is a catalyst that facilitates the curing reaction between the amine curing agent and the epoxy resin. The fumed silica acts as a nucleating agent and PEG-b-PPG-b-PEG as the foam stabilizer. The curing reaction between amine and epoxy resin results in a strongly crosslinked three-dimensional foamed network, as shown in Figure 1.

Thermal decomposition, foaming and curing of epoxy and other properties: The decomposition temperature of B-DDCM at which CO2 is released was characterized using differential scanning calorimetry (DSC). The DSC analysis revealedshowed that B-DDCM starts to release CO2 near 80, indicating the initial stage of decomposition (and foaming). As ambient temperature increased, the decomposition maximized at 125, as indicated by the minimum of the endothermic peak (Figure S1).

The foaming and curing processes of the resin mixture were measured and monitored in-situ using a parallel plate rheometer (TA Instruments Discovery HR-2) equipped with an Environmental Test Chamber. The resin mixture was tested with an oscillation temperature ramp for which the dynamic moduli, including the storage and loss moduli (G′ and G″), were measured as the temperature was increased at a rate of 5 from 50 to 180. The influence of the catalyst was evaluated through comparative experiments conducted in its presence and absence (Figure S2, S3). The structure of tertiary amine catalysts significantly influences the curing kinetics and reactivity of epoxy/dicyandiamide systems ([11]), highlighting the importance of catalyst selection in optimizing epoxy resin performance. The catalyst used here was 2,4,6-

tris(dimethylaminomethyl)phenol. As shown in Figure S2, with the catalyst, G′ and G″ started dropping (indicating onset of foaming) at 80, followed by large data fluctuation corresponding to release of CO2 which creates rheological instability within the resin sample. As the temperature continued to increase, G′ and G″ started to increase, indicating the progression of the curing reaction. A plateau was reached at 160 as curing was completed and a rigid foam was formed. In comparison, without the catalyst, both foaming and curing occurred at temperatures of about 10 higher. The catalyst played two roles, decreasing the decomposition temperature of B-DDCM and increasing the curing rate at lower temperatures. The addition of the catalyst also reduced the viscosity of the resin, allowing it to flow more easily during injection and reach target zones before activation. This reduction in viscosity can be seen from the lower G′ and G″ with the catalyst in the temperature range of 50 to 80 before foaming.

Resin injection scenarios: we evaluated two primary modes of resin injection into fractured geothermal fields: (i) injecting resin fronts designed to be displaced and directed into highly permeable fractures using packers to localizing, which enable localized annular injection and promote preferential flow paths; and (ii) injecting small resin droplets, sized to facilitate long-range transport through fracture networks, carried by the injection fluid. Based on preliminary laboratory experiments in simple fracture models, we concluded that the displacement patterns and control of resin fronts is impractical due to the high viscosity ratio between water and the resin (even with silicon oil as carrier due to the high temperatures > 100 in these early experiments). Consequentially, we focused on using resin droplets (generated and injected via special junctions that induce hydrodynamic instabilities and produces similar sized droplets). The injection of swarms of droplets (as experiments and theory show) offered better control over the transport and offered higher likelihood of altering high permeability zones away from an injection well (with less resin volume). This configuration of resin injection as droplets require special theoretical considerations of transport and activation of discrete sticking events that cumulatively modify the permeability of target (short-circuiting) regions as discussed in the theoretical and experimental sections.

3. LABORATORY EXPERIMENTS

The laboratory experiments focused on injection of epoxy resin droplets into model rock fractures with a portion of the model fracture heated to an activation temperature of 120, where resin droplets undergo foaming (expansion) and subsequent curing, thereby reducing local permeability within the model fracture. The laboratory-scale setup was designed to represents a single active fracture within a fractured rock of an EGS with constant flow rate of carrier fluid (silicon oil in the experiments report here) and an elevated environmental temperature mimicking natural geothermal field at moderate temperatures to ensure resin activation (and keeping a safer working environment).

We constructed several versions of simple fracture models with fixed apertures (ranging from 0.75 to 1.50) using aluminum plate at the bottom and cover glass glued with heat resistant silicon adhesive to withstand temperatures of 230. As shown in Figure 3, two classes of experimental fracture model designs were considered: (1) smooth fixed aperture models, and (2) fixed aperture fracture model with obstacles to mimic heterogeneity in the aperture plane. All models were constructed using machined aluminum plate at the bottom selected for ease of machining, superior heat conduction, and wettability properties similar to aluminosilicate igneous rock components (e.g. feldspars). Additionally, we constructed a u-shaped aperture model to extend effective length and amplify pressure drop signal. We verified using numerical simulations that the measured permeability of the fracture models was comparable to predictions for the same apertures (including obstacles and u-shaped model configurations).

The laboratory experiment setup, shown in Figure 4, consists of a flow loop driven by a peristaltic pump for circulating silicone oil (viscosity of 50 at 25) as the carrier fluid. Given that aqueous fluids are unsuitable at high temperatures under atmospheric conditions, silicone oil was selected for its thermal stability. Also, silicone oil is chemically highly inert and has no reaction with other components due to polarity mismatch. A peristaltic pump established steady state flow of silicon oil into which resin droplets were injected (using

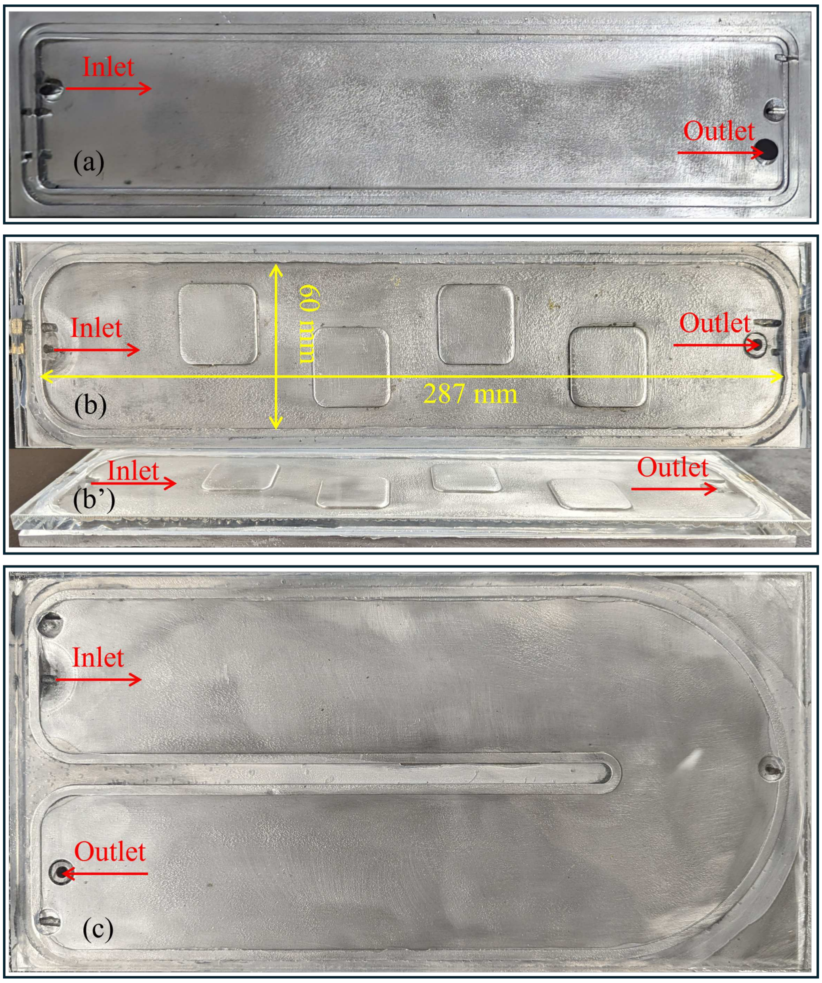

Figure 3: Images of fracture models used in laboratory experiments. (a) Model 01: fixed aperture model, b = 1.50; (b) Model 02: fixed aperture model with four round square obstacles, b = 1.50; (b') An oblique view of Model 02 with top glass cover attached; (c) Model 03: u-shape fixed aperture model (double the length of other fracture models), b = 0.75.

t-junction and coaxial injection setting) [9, 28]. The model rested on a heated plate (Guardian 5000) to control temperature in the fracture and induce foaming of the resin (the plate temperature was 160 during experiment). The process was monitored from above using both standard video and infrared cameras to capture the behavior of the injected resin droplets, including their displacement, foaming, and curing patterns.

Each experiment was initiated by circulating silicon oil through the liquid loop and measuring pressure drop across the fracture model while the temperature of the heating plate was raised to 160 (the temperature was higher than the threshold to account for vertical thermal gradient and heat losses). A constant flow rate of about 40 was maintained. Droplets were then injected into the loop from the injection port using a syringe pump (Fusion 200) at a rate of 0.05. The droplets size vary with the injection outlet diameter and flow rate of shearing liquid; typical droplet size in the experiments reported here was less than 0.75 to ensure passage through all inlets and outlets of the system. This resin injection rate is also low enough to avoid the interaction between droplets, correspond to the low dose of resin injection in the real geothermal field. A sink tank with filter is used for silicon oil cooling and inactivated droplet collection. The flow of the droplets into the model and their transformation and expansion were recorded using high resolution (1920 × 1080 DPI) video camera at rate of 30. During the transport, sticking and expansion of the resin, we monitored changes in pressure drop across the fracture model using two high precision

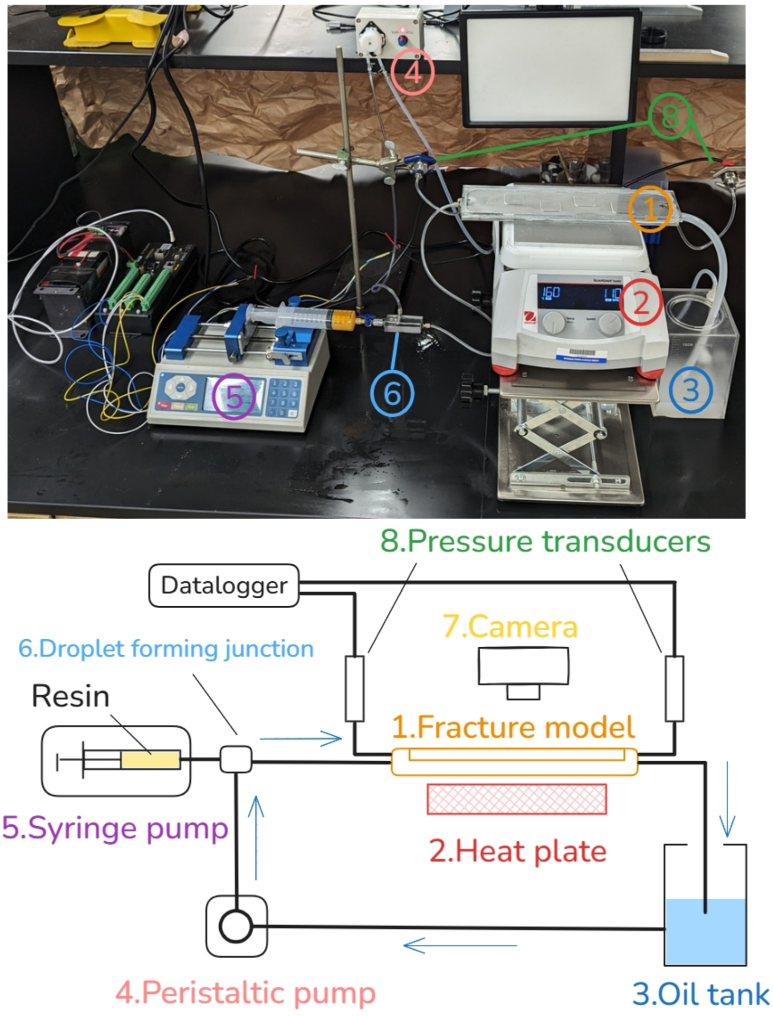

Figure 4: The components of the experimental setup used for laboratory experiments (top) and a schematic of main flow loop and other components of the setup (bottom).

pressure transducers (Omega PX191-200GV5) connected to a CR1000Xe datalogger. Experiments lasted (typically 2-3 hours) until silicon oil flow was practically blocked or pressure at the inlet reached values that deemed too risky (> 50).

4. NUMERICAL MODELING

We developed a two-dimensional Stokes fluid model to simulate the flow field within a single fracture and represent individual droplet transport, sticking to hot surfaces and expansion including dynamic feedback of reducingand dynamic effects on local aperture and permeability. We focus on the velocity field for the middle plane of fracture apertures, as shown in Figure 5. The numerical model implements a modified Stokes equation to describe incompressible flow between two quasi-parallel surfaces [14, 16]. The injected resin droplets are passively transported by the background carrier fluid. When the droplets reach a prescribed temperature along their path, they release CO2 blockers causing foaming and in-situ curing. The model represents this process by making the droplets stick and expand to locally reduce the fracture aperture in proportion to expanded droplet volume as shown in Figure 5. We implemented a stochastic sticking process that considers both the fracture geometry and the droplet state. The model predicts adhesion of resin droplets to fracture surfaces based on a stochastic function aware of local aperture, droplet size and temperature (as discussed below). As droplets adhere and undergo volume expansion,

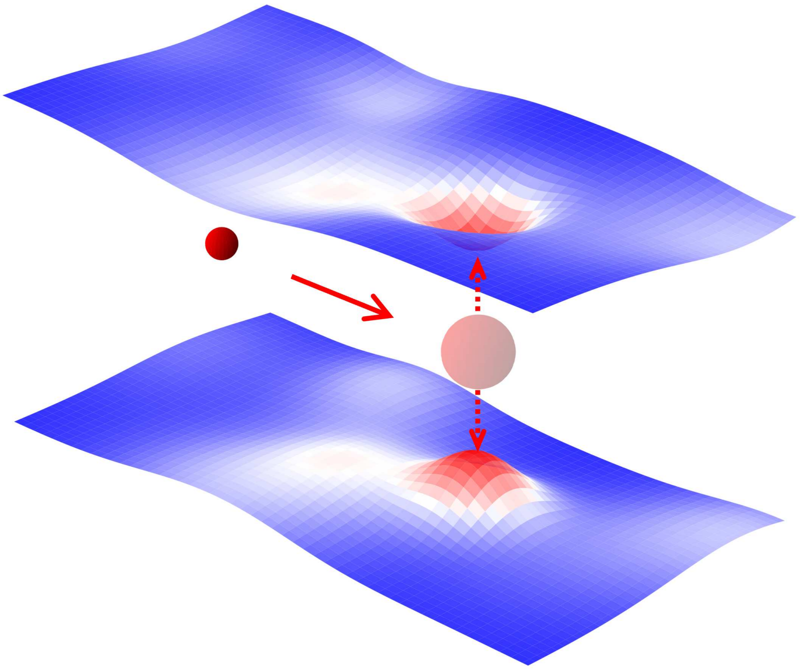

Figure 5: A conceptual depiction of a quasi-parallel wall fracture simulation domain. The blue planes represent the top and bottom fracture surfaces, a resin droplet (red) attaches to the red peak to smoothly alter local aperture. Aperture alteration is achieved by symmetric division of the expanded resin droplet volume between top and bottom to create a local gaussian shaped narrowing of the aperture (smoothness is essential for the 2-D simplification of the 3-D flow field).

they reduce the local fracture aperture and restrict flow pathways thus decreasing the fracture's overall permeability.

Depth-integrated flow model: In many practical applications, especially those involving thin geometries or planar domains, fully three-dimensional flow modeling can be computationally intensive and unwarrantedunnecessary. A key aspect of simplifying the Stokes flow equations involves collapsing the three-dimensional flow field into a two-dimensional form. We assume that fracture aperture vary gradually such that the velocity normal to the fracture walls is approximately zero ($u_n \approx 0$) and viscous forces in the flow field are dominated by shear forces acting normal to the fracture wall ($\nabla^2 u \approx \partial^2 u / \partial n^2$). Incorporating these velocity conditions into the Stokes equation and assuming that the fracture walls are approximately normal to the z-axis yields:

$$0 = \mu \frac{\partial^2 u}{\partial z^2} - \nabla p \tag{1}$$

where $u = (u_x, u_y, 0)$ is a three-dimensional velocity vector with a direction parallel to the x-y plane. Incorporating the no-slip condition ($u = 0$) at the fracture walls, Equation. 1 is integrated across the local aperture ([34]) yielding:

$$u(x, y, z) = u_m(x, y)\,(1 - \frac{z^2}{(b/2)^2}) \tag{2}$$

where u_m is the velocity at the middle plane, and $b = b(x, y)$ is the local aperture. The velocity satisfies a parabolic profile in the z direction, while $u = u_m$ when $z = 0$. The velocity and the velocity goes to zero when $z = \pm b/2$.

For a typical rock fracture, the aperture size (~ 0.1) is much smaller than its length scale in flow direction (> 1) ([1]). In this study, we focus on fluid velocity field for fracture mid plane, as shown in Figure 5 for two quasi-parallel plates. Based on these conditions, the integration of 3D Stokes equation over z axis in range $(b, -b)$ becomes:

$$\begin{aligned}\frac{2}{3}\frac{\partial^2(2bu_{xm})}{\partial x^2}+\frac{2}{3}\frac{\partial^2(2bu_{xm})}{\partial y^2}-\frac{4}{b}u_{xm}-\frac{\partial(2bp)}{\partial x}=0\\ \frac{2}{3}\frac{\partial^2(2bu_{ym})}{\partial x^2}+\frac{2}{3}\frac{\partial^2(2bu_{ym})}{\partial y^2}-\frac{4}{b}u_{ym}-\frac{\partial(2bp)}{\partial y}=0\end{aligned} \tag{3}$$

where the coefficient $2/3$ of the first two terms is due to the volume flux with parabolic velocity profile (it is $2/3$ of the volume flux with uniform profile and mid-plane velocity u_m). The third term acts as a friction term, representing friction forces due to upper and lower fracture walls.

Since we do not invoke any source terms, the continuity equation is unaffected by the velocity profile assumption (parabolic or otherwise). The conserved quantity changes from velocity to the product of velocity and local aperture.

$$\frac{2}{3}\frac{\partial(bu_{xm})}{\partial x}+\frac{2}{3}\frac{\partial(bu_{ym})}{\partial y}=0 \tag{4}$$

Transport and adhesion of resin droplets: In previous sections we discussed the preferred configuration for introducing heat-sensitive resin in the form of droplets that are expected to be convected with the carrier fluid. Upon reaching the target thermal conditions within the EGS heat exchange region, the resin droplets are expected to adhere to fracture surfaces, expand as they foam, and subsequently cure to reduce permeability. The droplet adhesion process is influenced by multiple factors, including droplet size, morphology, surface roughness, and temperature etc. In the present study, the droplet state (specifically before and after foaming) also significantly affects adhesion behavior. In the simulation model, droplet adhesion is treated as a stochastic process. At each time step, a droplet possesses a defined sticking probability. During simulation, a uniformly distributed random number is generated; if this value falls below the sticking probability, the droplet undergoes fixation. When the sticking probability remains constant over time, the spatial distribution of droplet adhesion events follows a geometric distribution.

Once a resin droplet is triggered to stick via the stochastic process, it transforms into a localized bump on the fracture surface. This transformation is shown in Figure 5. Between two quasi-parallel fracture surfaces (blue planes), the resin droplet (red sphere) transforms into two symmetric bumps, one on each surface (top and bottom). The symmetric assumption is incorporated in depth-integrated flow model. The transformation conserves volume, with the total volume of the original resin droplet equal to the combined volume of the resulting two bumps. Each bump is modeled as a 2-D Gaussian shape, with a height equal to the radius of the original droplet. The Gaussian profile is selected for its smoothness which is required for implementation of Equations 3 and 4.

We use a simple scaling law to estimate droplet sticking probability P by assuming that sticking probability is proportional to the droplet collision frequency f with walls. This leads to the sticking probability becoming proportional to the droplet velocity u_d and inversely proportional to the difference between the local aperture and droplet diameter (i.e., small droplets in large fracture aperture have lower sticking probability), as:

$$P(x,y,d)\sim f\sim\frac{u_d}{b(x,y)-d} \tag{5}$$

The droplet diameter in simulation followed normalized distribution $d\sim\mathcal{N}(d_0, d_0/10)$, where d_0 is the mean droplet diameter within experiment. Also from the experiment, we can calibrate mean droplet sticking probability $P_0 = P(d = d_0)$. The sticking probability for droplet under other injection scenario can be calculated by Equation 5. In a subsequent study, we will report more rigorous testing of the statistical

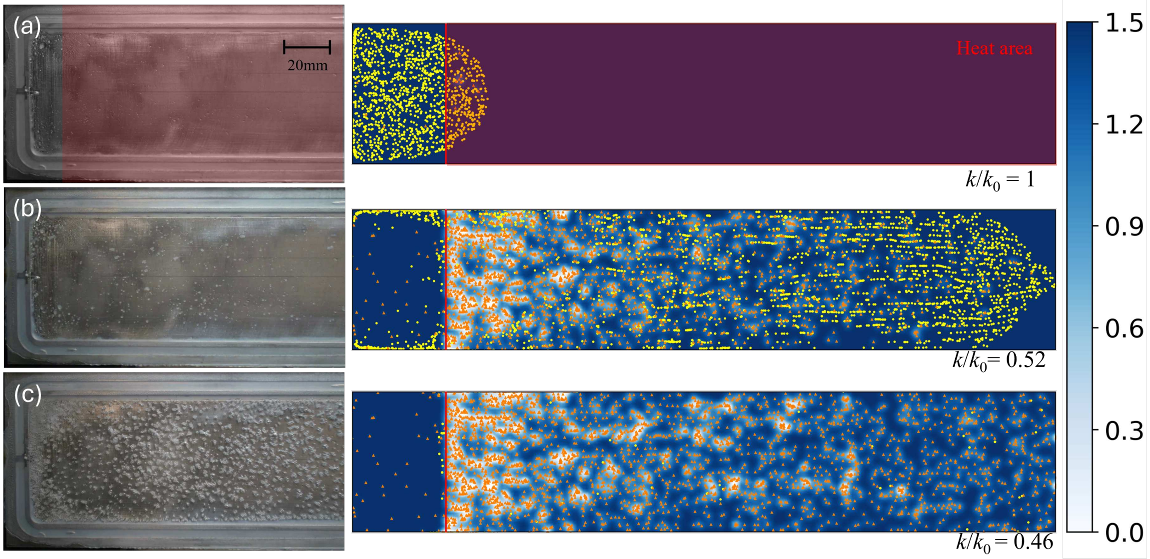

Figure 6: Images from laboratory experiments (left) compared with simulation results of resin droplet attachment (right) forat the similar stages of droplet injection. The droplets in motion are marked by yellow dots for droplets in moving and change to orange color for attached resin droplets. The panels (a), (b), and (c) represents different stages during the experiment, (a) beginning of resin droplet injection, (b) for the stage where droplets become attached, and (c) for the distribution of foamed resin droplet at the end of injection. The heated section of the domain for both experiment and simulation is marked by red color in (a). For the simulation results images, aA droplet crossing the red line (heated region above thermal activation threshold) is expected to become activated and eventually adhere to the surface (following aaccording to sticking probability, P_0), the attached resin droplet thenand subsequently expands up to 10 times its original volume with commensurate changes in local fracture aperture (marked by athe color field from original aperture in blue to blocked region in white). Overall changes in fracture permeability k (based on simulation results) are noted on simulated images.

behavior of a swarm of droplets in a fracture network. For this study, we demonstrate feasibility of this ad-hoc sticking probability relations in the numerical results shown in the next section.

5. RESULTS

5.1. Numerical Model

For comparison, a simulation was conducted using a domain similar to the experimental setup. A total of 7,000 droplets (diameter $d \sim \mathcal{N}(b/10, b/100)$) were progressively released from a line source at the fracture inlet. The average droplet sticking probability was set to $P_0 = 85\%$, meaning that 85% of the droplets are expected to adhere to the fracture walls within 1.

The Figure 6 shows qualitative comparison between laboratory experiments and simulations at similar stages of droplet injection. The right panel shows how the aperture field (initially set to 1.50) changes with adhesion and expansion of resin droplets with white regions marking smaller local apertures due resin droplet attachment and expansion. The resin droplets (yellow dots) are transported by the flow and expand after passing the heated region of the fracture (marked by red line). Each droplet has a defined sticking probability during transport, and once attached, it is marked as an orange dot. These adhered droplets modify local aperture, representingrepresnting resin droplet sticking behavior observed in laboratory experiments (shown in next section). At the end of simulation, the model permeability k decreased to half of its initial permeability k_0. In the intermediate stage shown in Figure 6(b) right, downstream alignment of 'droplet lines' is observed. This alignment arises because earlier-attached droplets locally alter the fracture aperture, thereby guiding the paths of following droplets and inducing spatial organization.

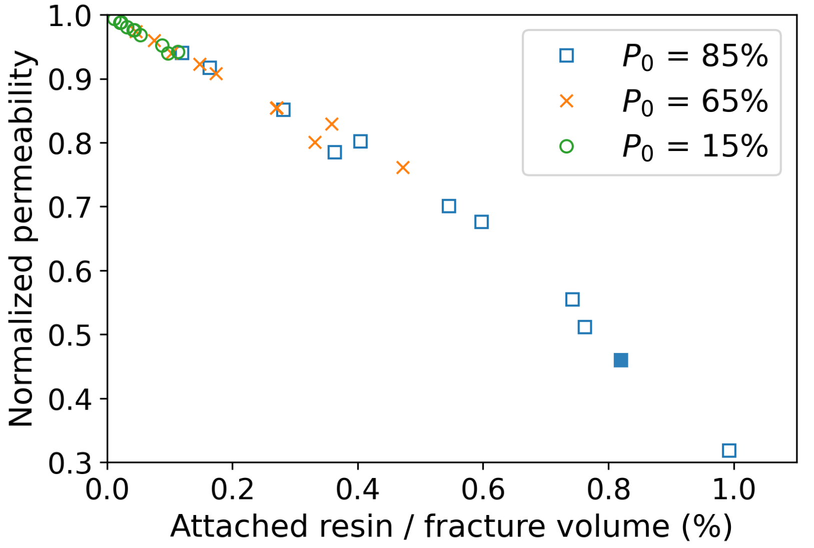

Figure 7: Normalized permeability changes with fraction of attached resin droplet volume scaled by the total model fracture volume for different values of mean droplet sticking probability P_0. The solid square indicates the simulation result depicted in Figure 6(c)

AdjustingBy adjusting the total number of droplets (1000 to 20000) and their mean probability of sticking, P_0 = 15%, 50%, 85%, Figure 7 shows thatvariations in fracture permeability is reduced (nearly linearly) with the fraction of attached droplet volume irrespective of details of the attachment dynamics(nearly linear relations). The results in Figure 6 also illustrate details ofvisually show internal feedback where droplet adhesion affects subsequent adhesion behavior. ImportantlyMore importantly, the simulation results highlight the potential efficacy of the proposed method for altering fracture permeability alteration with relatively small volumes of injected resin. Based on the numerical results in simple settings of a single fracture, we note that **relatively small volumes of attached resin droplets (0.2% of the fracture volume) may result in over 10% decrease in fracture permeability**. Evidence suggests (see experimental section), that an order of magnitude reduction in fracture permeability is possible with about> 1% volume reduction due to the distributed nature of attached resin droplets. Moreover, the process is not sensitive to details of droplet sticking probability, only to the cumulative volume of attached resin droplets implying that prolonged resin injection campaigns using low density of resin droplets can achieve the desired permeability alterations. Following additional calibration of the numerical model, we will use the model to explore resin droplet dynamics within large-scale fracture networks and emerging behaviors that, at present, are challenging to investigate experimentally.

5.2. Laboratory experiments

An illustrative example of the transformation associated with resin activation and foaming of mm-scale resin droplets on the hot section of a fracture model (surface temperature 160°C) is depicted in Figure 8. Within two minutes, the resin droplets carried by silicon oil exhibit noticeable volume expansion and evidence of foaming due to CO2 bubbles entrapped in the epoxy resin (and subsequent curing and hardening). In laboratory experiments, a fraction of the resin droplets that may undergo foaming may be carried by the flow out of the fracture model before adhering to the surface. Through image analyses, thresholding the continuous frame images to binary mask, the centroid and shape information of resin droplets can be extracted. The identified resin droplets are tracked by particle tracking algorithm ([2]) to avoid repeat count. We summarize the droplet volume distribution in Figure 8(c) for experiments within Model 01 (b = 1.50). The droplet volume is estimated by its projected area. The droplets are counted selectively when projected area is larger than 4 pixel^2 (≈ 0.1) and diameter smaller than 1.00 (inlet tube diameter).

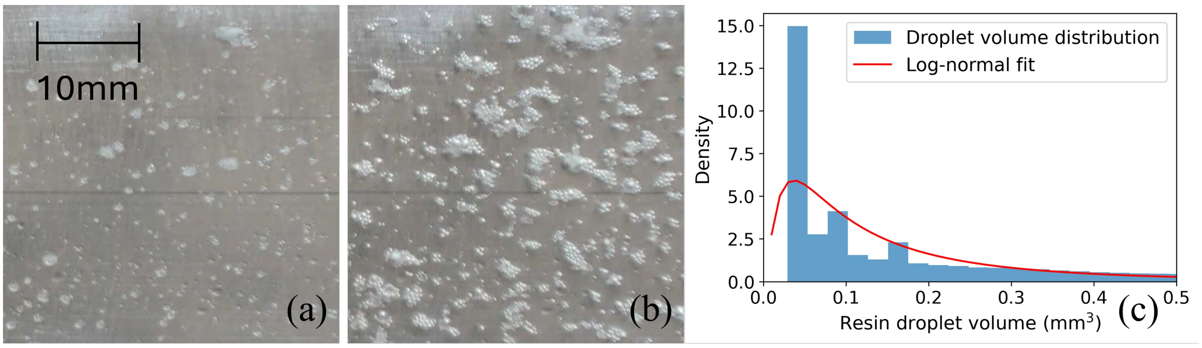

Figure 8: Resin droplets before (a) and (b) 120 s later showing foaming and volume expansion on a hot section of a fracture model. (c) resin droplet volume distribution within the model generated by coaxial tube junction within fracture Model 01, b = 1.50.

For the experiments reported in this study, we generated resin droplets using a coaxial tubing junction [28, 7]. Based on the viscosity ratio between the disperse phase (resin mixture) and continuous phase (silicone oil), we can control the generated resin droplet size and frequency by adjusting the flow rate ratio and channel diameter ratio. In our current experiments, the coaxial tubing junction consists of a 14G blunt-tip needle (outer diameter 2.10) as the inner channel and a 2.74 drilled well in a plastic block as the outer channel. Most of the resin droplets generated had a volume of approximately 0.05 ($d \approx 0.5$).

The core of the experimental results reported in this study are shown in Figure 9 which illustrates dynamic changes in liquid pressure drop in the fracture model and slight variations in silicone oil injection rates during the experiment. The preheat process start with silicone oil cycling in the system. The increased temperature of the circulating silicone oil resulted in a decrease in the oil viscosity and a reduction in the pressure drop with an increase in flow rates. After approximately 40 minutes, the silicone oil flow rate reaches a steady state of about 40 and measured pressure drop across the model stabilizes at around 3 as for Model 03. At this point, we begin with epoxy resin injection. The initiation of resin droplet injection is marked as time 0. During the resin injection phase, the pressure drop increases exponentially from 3 to 30 due to adhesion of droplets within the model fracture aperture and their subsequent foaming. Even after the resin injection ceases, the pressure drop continues to increase as the epoxy resin foams and expands within the model, eventually stabilizing at approximately 40.

Figure 10 depicts the commensurate changes in the permeability of three different fracture models as a function of resin injection. The permeability decreases exponentially by an order of magnitude as the resin foam blocks flow pathways, with no more than 8 of resin mixture injected (The total volume within the model is 15 to 25). During the initial stage of resin injection, the majority of resin droplets that entered the fracture model were swept away by the flow, with only a small fraction adhering to the fracture surfaces. As droplet adhesion occurs, the flow pathway becomes increasingly complex, promoting further droplet adhesion. The two fracture models with 1.50 apertures exhibited similar initial permeability, but the model with square obstructions experienced a faster permeability decline. In contrast, the model with a 0.75 aperture shows a comparable rate of permeability reduction to the 1.50 square-aperture model. This similarity likely arises from their identical cross-sectional area in the direction of flow, as the square obstructions have half the width of the main channel (see Figure 3).

6. LIMITATIONS AND CHALLENGES

While our laboratory-scale experiments provide important insights into resin droplet transport, deposition, and blockage mechanisms under controlled conditions, real-world geothermal reservoirs present additional layers of complexity. The controlled geometry and flow conditions in single-fracture models allow for systematic observations towards developingand mechanistic understanding, howeverbut natural fracture networks are inherently more heterogeneous and dynamically coupled. Consequently,

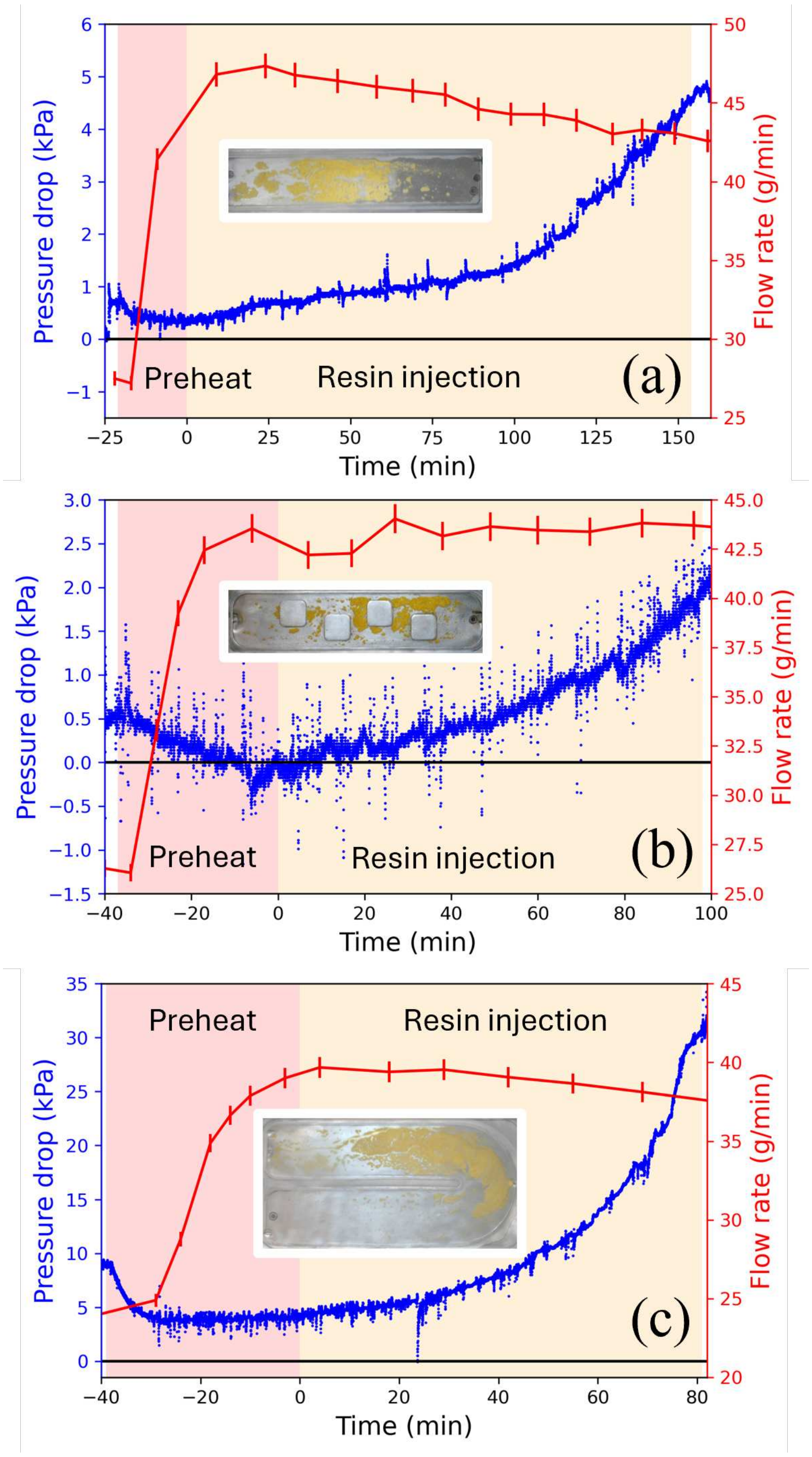

Figure 9: Variations in pressure drop and silicon oil injection rates over time in a representative set of experiments with corresponding fracture model images with foamed resin at the end of experiment (flow direction from left to right). The "preheat" and "resin injection" stages are indicated by red and orange backgrounds (a) Model 01, b = 1.50; (b) Model 02, b = 1.50; (c) Model 03: u-shape, b = 0.75.

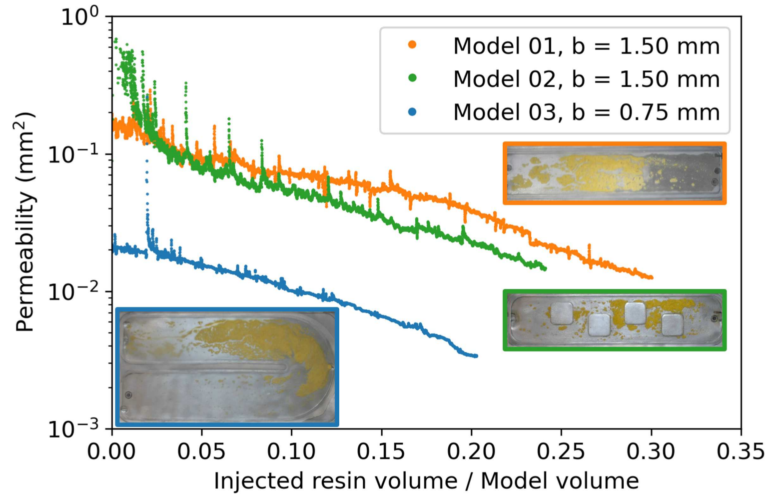

Figure 10: Measured changes in fracture model permeability with normalized injected resin volume (resin volume / total fracture volume) for different fracture models corresponding to experimental results in Figure 9.

the translating findings of these idealized experiments to field-scale applications are not straightforwardsystems introduces several important limitations and challenges. The upscaling of our laboratory observations of droplet behavior from a single fracture to natural fracture networks is challenging in part due to topological complexity and the potential droplet screening and entrapmentdroplet entrapment in natural fractured media. The natural tendency of resin droplets to coalesce is likely to be influenced by interactions with upstream neighboring and already entrapped resintrapped droplets. Likewise, the heterogeneous flow fields that naturally arise in fracture networks canmay produce velocity variations inacross orders of magnitude, even when apertures are uniform due to complex internal geometry and fracture intersections that are likely to affect droplet migration, breakup, and expansion, thus posing a major challenge for prediction ofaccurately predicting travel distances and clogging behavior at larger scales. The nonlinearities of droplet's transport distance and sticking probabilities as a function of fracture aperture and flow rates are difficultmay be hard to capture with simple upscaling or averaging techniques at the network scale. Blockages in an individual fracture or at certain critical junctions may have a disproportionate effect on global permeability of the geothermal field, depending on the redundancy and connectivity structure of the network. Since scaling laws derived from single-fracture models may not directly apply to complex fracture networks, ensemble simulation approaches may be oversimplified masking mechanisticrisk oversimplifying or diluting the detailed mechanistic insights gained from idealized single-fracture studies. Scale-aware multiscale modeling approaches may become essential to properly incorporate network topology, heterogeneous flow, and nonlinear transport behavior to bridge the gap of droplet transport between single fracture models and large-scale network behaviors.

Further, the experiments under atmospheric pressure conditions are of limited value when considering the transport and volume changes of the resin under high fluid pressures expected at depths of natural EGS settings (22 km to 3 p). High liquid pressuresliquidressures may affect the kinetics and extent of droplet expansion and curing, the use of water as a carrier liquid has not been tested (due to the high temperatures) and thus hydrodynamic behavior of the resin under these conditions is largely unknown. We have established activation temperatures, rheological and mechanical behavior of the resin under atmospheric conditions, we should expect different foam morphology and probably mechanical properties under high pressures. In summary, the evaluation of the concept under atmospheric conditions in a simple fracture model is encouraging, yet this is not more than a preliminary proof of concept and more rigorous testing would be needed before testing under field conditions would be possible.

7. SUMMARY AND OUTLOOK

The design and operation of modern geothermal fields borrow heavily from advances in petroleum engineering such as the use of horizontal parallel wells in the Fervo project in North-Central Nevada [24, 18]. These modern drilling and field operations can suffer from flow concentration during fracking and also due to induced seismicity [18]. The concept of using heat-activated resin droplets that can expand at target locations (based on prescribed activation temperature) and adhere to surfaces offers a novel solution to addressing such unintended concentrated flows that might affect EGS performance and economic viability. In this study, we describe the synthesis and properties of the heat-activated epoxy resin and preliminary tests of its properties and chemical "levers" for attaining different viscosity and activation temperatures.

The preliminary laboratory tests demonstrated the viability of the approach for simple fracture models, showing an order of magnitude reduction in permeability reduction for reasonable injection scenarios. We emphasize that these tests were performed under atmospheric pressure and not the high pressure conditions expected in standard EGS applications (2 to 3), nor subjected to the complex flow topology of natural fractured rock. Additional complications may arise due to the behavior of natural carrier liquid (water), however, since the resin is immiscible in aqueous solution (as in the experimental silicon oil), these difference may not be critical for field applications.

Fracture network aspects are being investigated numerically and experimentally and will be reported in a future study. The new method offers a promise of addressing cm-scale fractures not easily addressed with present permeability alteration methods [10, 20]. Droplet formation for field injection protocols needs to be refined to ensure sufficient travel distances without premature screening of the droplets. The numerical results offer insights into the robustness of the injection strategy in which the alterations are cumulative and can be induced over long resin injection campaigns at low resin volumes (or droplet density in the carrier liquid).

Acknowledgments

We gratefully acknowledge DOE funding for "Modification of Fractured Rock Permeability Field Using Polymer Foam to Improve Geothermal System Efficiency" (DE-SC0023426) awarded to UNR and DRI.

Author Contributions

Dani Or conceptualized the research framework and supervised the overall project. **Yutong Cui** developed the numerical model and established the laboratory experiment. **Dani Or** and **Yutong Cui** jointly interpreted the results and co-wrote the manuscript. **Ying Yang** and **Manish Bishwokarma** contributed to the heat-activated foam experiments and drafted the corresponding section. **Rishi Parashar** and **Satish Karra** provided supervision and technical guidance on the fracture simulation. All authors reviewed and approved the final version of the manuscript.

ORCID IDs

Dani Or	https://orcid.org/0000-0002-3236-2933
Rishi Parashar	https://orcid.org/0000-0002-9733-7309
Ying Yang	https://orcid.org/0000-0001-8980-1776
Manish Bishwokarma	https://orcid.org/0009-0002-6700-8886
Satish Karra	https://orcid.org/0000-0001-7847-6293
Yutong Cui	https://orcid.org/0000-0000-0000-0006

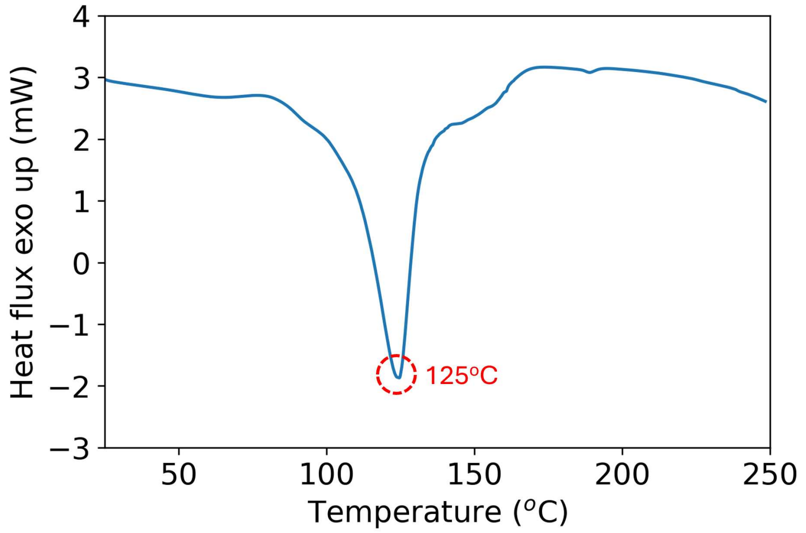

Figure S1: DSC curve of CO2 blocked amine crosslinker (B-DDCM) measured at a constant heating rate of 5 showing that the B-DDCM started to release CO2 near 80 and reached the maximum decomposition rate at 125 as indicated by a minimum of the endothermic peak (see main text for details).

A. HEAT ACTIVATED EPOXY RESIN FOAM

In this appendix we summarize details of the heat-activated resin foaming, curing rate, mechanical strength and ability to withstand thermal degredation. First, we evaluated the critical temperature for peak foaming (release of CO2) when the resin travels from ambient temperatures to elevated temperatures in a geothermal field. The thermal stability of the CO2-blocked amine crosslinker B-DDCM was characterized using differential scanning calorimetry (TA instruments DSC Q100) as depicted in Figure S1. The sample was heated at a heating rate of 5 from 25 to 250. The results showed that CO2 gas release started at around 80 and as temperature increased, resin activation reached the maximum at 125 as indicated by the minimum of the endothermic peak (Figure S1). We thus established the critical temperature for activation of the heat-sensitive epoxy to be approximately 125.

In several experiments, we observed that at 125 without using a catalyst, the curing rate was slow relative to the rate of gas release causing loss of CO2 bubbles from the resin and resulting in collapsing of the foamed resin and lower volume expansion. This phenomenon is attributed to a rapid foaming rate without sufficient increase in resin stiffness (or curing). To accelerate the rate of curing, we added 2,4,6-tris(dimethylaminomethyl)phenol as a catalyst [11]. The catalyst not only improved CO2 bubble retention within the foam, but also improved the overall thermal stability of the stiff foam. The effects of the catalyst on curing kinetics were analyzed using a rheometer (TA Instruments Discovery HR-2). The resin mixture was loaded onto the 25 stainless steel parallel plates and tested with an oscillation temperature ramp for which the dynamic moduli, including the storage and loss moduli (G′ is the elastic component and G″ the viscous component), were measured as a function of resin temperature. The results are shown in Figure S2. For an epoxy resin containing 1 wt.% of catalyst, both G′ and G″ show a drop around 80, followed by large fluctuations while moduli drop to the minimum (these reflect resin foaming before curing). As temperature continued to increase at a rate of 5, G′ and G″ started to increase, indicating curing. A plateau was reached at 160 where curing was completed and a rigid foam was formed. The catalyst induced an earlier release of CO2 (the stiffness levels were similar as seen in Figure S2). To show the enhanced rate of curing reaction in the presence of the catalyst, we conducted an isothermal time sweep, where the temperature was kept at 90 and G′ and G″ were measured as a function of elapsed time (Figure S3). Without the catalyst, foaming was observed from the fluctuation of the dynamic moduli. The

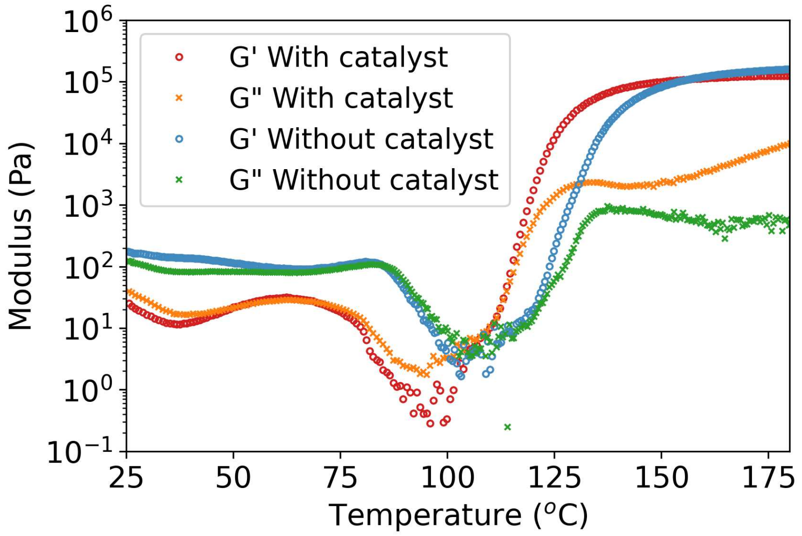

Figure S2: Storage modulus (G') and loss modulus (G'') as a function of temperature for the resin mixture with and without catalyst at a heating rate of 5, a frequency of 1, and an amplitude of 0.1% strain.

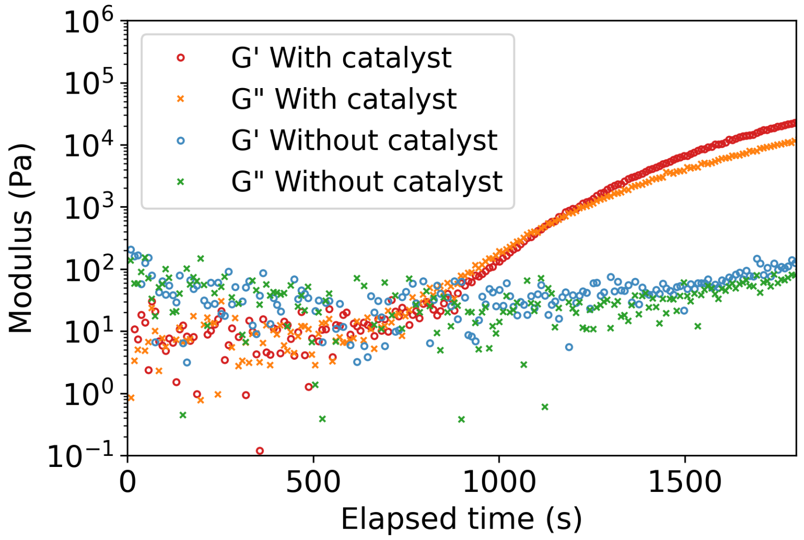

Figure S3: Isothermal time sweep at 90 with an amplitude of 0.1% strain and a frequency of 1 showing the change of storage modulus (G') and loss modulus (G") for the resin mixture with catalyst and without as a function of time.

release of CO2 nearly completed after 1800 without any indication of curing. With the catalyst, curing took place at 600 shown by the increase of G′ and G″.

We therefore have used the catalyst throughout the experiments reported here. The epoxy foam formed by heating in an oven at 125 for one hour was subjective to compression test using Shimadzu AGS-X testing frame at a rate of 5. The compressive strength at the plateau region was 1.0 at 14% strain as shown in Figure S4. The plateau region represents the stress level at which the foam mechanically collapses under compression.

We also evaluated the thermal stability of the epoxy foam using thermogravimetric analysis (TA Instruments TGA Q50) with a temperature ramp from room temperature to 400 at a heating rate of 5. As shown in Figure S5, the foam remained thermally stable up to 280, with no detectable mass loss

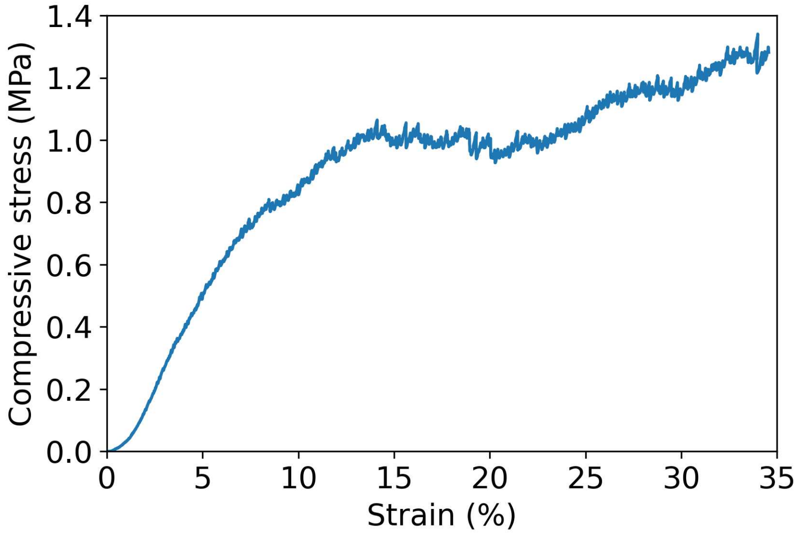

Figure S4: Compressive strength of the epoxy foam measured at room temperature with 5 compression rate.

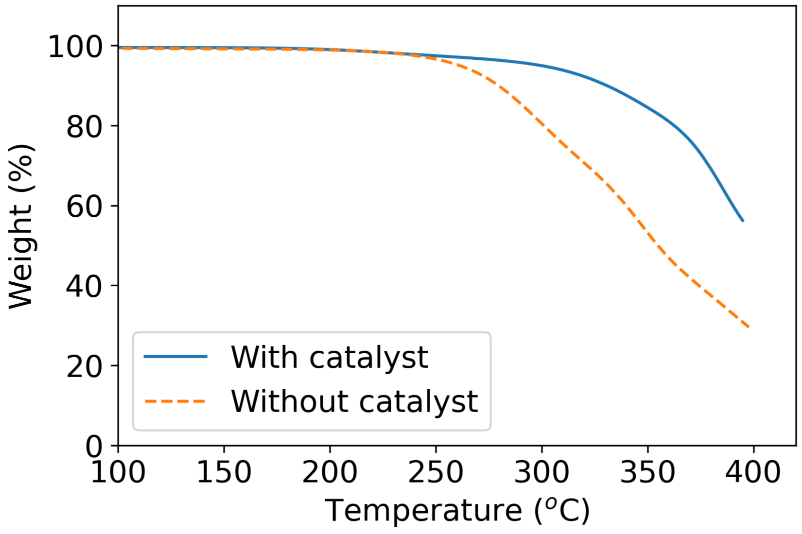

Figure S5: Thermogravimetric analysis (TGA) results for the epoxy foam with and without the catalyst at 5 heating rate showing the increase of 5% weight loss temperature from 280 to 300 upon adding the catalyst.

under (N2) atmosphere. The inclusion of catalyst increased the degradation onset temperature, shifting the 5% weight loss point from 280 to 300.

B. FRACTURE MODEL PERMEABILITY MEASUREMENTS

Prior to the experiment, the permeability of each model was determined by measuring the pressure drop across the model at various prescribed flow rates, corresponding to Reynolds numbers ranging from 0.1 to 0.5. The setup uses for permeability measurements, shown in Figure 4, is same to the experimental configuration but conducted at room temperature (approximately 25). It consists of a closed-loop system driven by a peristaltic pump circulating silicone oil (viscosity η = 50 at 25). By measuring both the pressure drop and flow rate of silicone oil, the permeability k of the model can be calculated using:

$$k = v\frac{\eta \Delta x}{\Delta p} \tag{S1}$$

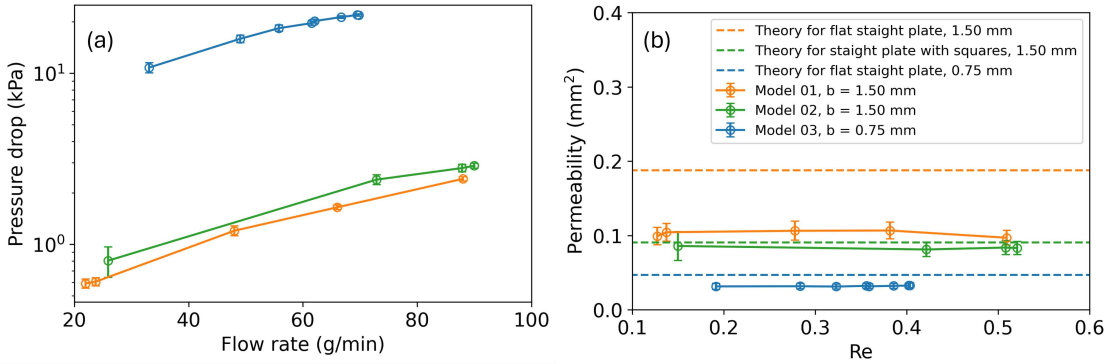

Figure S6: Permeability measurement for three different experimental models. (a) Pressure drop change with silicone oil flow rate; (b) Permeability change with Re number and corresponding theoretical permeability.

where v is the average flow velocity, $\Delta x \approx 280$ is the distance between model inlet and outlet, Δp is the pressure drop across the model.

For comparison, the theoretical permeability k_T between two infinite parallel plates is given by:

$$k_T = \frac{b^2}{12} \tag{S2}$$

where b is the aperture between the plates. For the model containing square obstacles, [17] provides an expression that relates the effective 2D permeability k_2 (only the viscous resistance of the fluid around the cylinder is considered) to the 3D permeability with obstacles k_{TO}:

$$k_{TO} = k_2 \, [1 - \frac{2\sqrt{k_2}}{\phi b} \tanh{(\frac{\phi b}{2\sqrt{k_2}})}] \tag{S3}$$

Where ϕ is the porosity of the model (the fraction of space in the model plane that is not occupied by obstacles). The hyperbolic tangent term accounts for additional shear resistance of the fluid in z-direction (through the thickness direction). The effective 2-D permeability k_2 can be estimated using a lubrication-type approximation for flow between adjacent cylinders, as derived by [32]:

$$k_2 = \frac{a^2}{3.34(1-\phi)} \, [1 - 1.10\sqrt{1-\phi}\,]^{\frac{5}{2}} \tag{S4}$$

where a is the radius of the cylinders. In our model, since the obstacles are rounded square, we use an equivalent radius to approximate their hydraulic effect.

Figure S6 illustrates typical values of fracture model permeability for 0.75 and 1.50 apertures (predicted and measured). The pressure drop ranged between 0.6 to 21.8 for flow rates in the range from 0.02 to 0.09 for the different fracture models. Measured permeability values remain nearly constant for all flow rates and fracture models. We note that measured permeability values for all models were lower than their theoretical counterpart probably due to resistances and flow behavior at the model entrances and aperture manufacturing errors. For the permeability of Model 03 (u-shape configuration) simulation results indicate that, for low Reynolds numbers (Re < 0.5), the permeability is comparable to a flat straight fracture with a similar aperture (i.e., the u-shaped flow field had little effect on the fracture permeability).

REFERENCES

1. Kevin Bisdom, Giovanni Bertotti, and Hamidreza M Nick. The impact of in-situ stress and outcrop-based fracture geometry on hydraulic aperture and upscaled permeability in fractured reservoirs. Tectonophysics, 690:63–75, 2016. `doi:10.1016/j.tecto.2016.04.006`.
2. Yutong Cui, Yang Zhang, Pan Jia, Yuan Wang, Jingcong Huang, Junlei Cui, and Wing T Lai. Three-dimensional particle tracking velocimetry algorithm based on tetrahedron vote. Experiments in Fluids, 59(2):31, 2018. `doi:10.1007/s00348-017-2485-9`.

3. Veronica D'Eusanio, Alessandro Girolamo Rombolà, Irene Coralli, Daniele Fabbri, Lorenzo Tassi, and Andrea Marchetti. Thermal degradation pathways in multi-component epoxy composites. Journal of Analytical and Applied Pyrolysis, 189:107107, 2025. `doi:10.1016/j.jaap.2025.107107`.
4. Cheikh Makhfouss Fame, Tamon Ueda, Marc A Ntjam Minkeng, and Chao Wu. Durability of epoxy and vinyl ester polymers in wet, seawater, and seawater sea sand concrete environments: Molecular dynamics simulations. Construction and Building Materials, 451:138645, 2024. `doi:10.1016/j.conbuildmat.2024.138645`.
5. Pengcheng Fu, Yue Hao, Stuart DC Walsh, and Charles R Carrigan. Thermal drawdown-induced flow channeling in fractured geothermal reservoirs. Rock Mechanics and Rock Engineering, 49(3):1001–1024, 2016. `doi:10.1007/s00603-015-0776-0`.
6. Bruce Gee, Robert Gracie, and Maurice B Dusseault. Multiscale short-circuiting mechanisms in multiple fracture enhanced geothermal systems. Geothermics, 94:102094, 2021. `doi:10.1016/j.geothermics.2021.102094`.
7. Ye Gu, Hiroyuki Kojima, and Norihisa Miki. Theoretical analysis of 3d emulsion droplet generation by a device using coaxial glass tubes. Sensors and Actuators A: Physical, 169(2):326–332, 2011. `doi:10.1016/j.sna.2011.02.043`.
8. Bin Guo, Pengcheng Fu, Yue Hao, Catherine A Peters, and Charles R Carrigan. Thermal drawdown-induced flow channeling in a single fracture in egs. Geothermics, 61:46–62, 2016. `doi:10.1016/j.geothermics.2016.01.004`.
9. Amit Gupta, SM Murshed, and Ranganathan Kumar. Droplet formation and stability of flows in a microfluidic t-junction. Applied physics letters, 94(16), 2009. `doi:10.1063/1.3116089`.
10. Iskander Gussenov, Nurxat Nuraje, and Sarkyt Kudaibergenov. Bulk gels for permeability reduction in fractured and matrix reservoirs. Energy Reports, 5:733–746, 2019. `doi:10.1016/j.egyr.2019.06.012`.
11. Mohammadnabi Hesabi, Ali Salimi, and Mohammad Hosain Beheshty. Effect of tertiary amine accelerators with different substituents on curing kinetics and reactivity of epoxy/dicyandiamide system. Polymer Testing, 59:344–354, 2017. `doi:10.1016/j.polymertesting.2017.02.023`.
12. Roland Horne, Albert Genter, Mark McClure, William Ellsworth, Jack Norbeck, and Eva Schill. Enhanced geothermal systems for clean firm energy generation. Nature Reviews Clean Technology, 1(2):148–160, 2025. `doi:10.1038/s44359-024-00019-9`.
13. Ernst Huenges. Enhanced geothermal systems: Review and status of research and development. Geothermal power generation, pages 451–473, 2025. `doi:10.1016/B978-0-443-24750-7.00012-9`.
14. Richard G Hughes and Martin J Blunt. Network modeling of multiphase flow in fractures. Advances in Water Resources, 24(3-4):409–421, 2001. `doi:10.1016/S0309-1708(00)00064-6`.
15. Maryam Khodayar and Sveinbjörn Björnsson. Conventional geothermal systems and unconventional geothermal developments: An overview. Open Journal of Geology, 14(2):196–246, 2024. `doi:10.4236/ojg.2024.142012`.
16. Rahul Krishna, Yves Méheust, and Insa Neuweiler. A two-dimensional depth-integrated model for immiscible two-phase flow in open rough fractures. Journal of Fluid Mechanics, 1011:A43, 2025. `doi:10.1017/jfm.2025.404`.
17. Sunil Kumar, Robert W Zimmerman, and Gudmundur S Bodvarsson. Permeability of a fracture with cylindrical asperities. Fluid Dynamics Research, 7(3-4):131–137, 1991. `doi:10.1016/0169-5983(91)90053-L`.
18. Greg Leveille. Hydraulically fractured horizontal wells: A technology poised to deliver another energy-related breakthrough of enormous scale. Journal of Petroleum Technology, 76(02):12–15, 2024. `doi:10.2118/0224-0012-JPT`.
19. Qiang Ma, Jingjie Lei, Jun He, Zhi Chen, and Wentao Li. Epoxy resin for solidification/stabilization of soil contaminated with copper (ii): Leaching, mechanical, and microstructural characterization. Environmental Research, 240:117512, 2024. `doi:10.1016/j.envres.2023.117512`.
20. Giuseppe Maddinelli, Martin Bartosek, Stefano Carminati, Leili Moghadasi, Nicolò Manfredini, and Davide Moscatelli. Design of thermoresponsive polymers to selective permeability reduction in porous media. In Abu Dhabi International Petroleum Exhibition and Conference, page D011S016R001. SPE, 2020. `doi:10.2118/203492-MS`.
21. Matthew L McLean and D Nicolas Espinoza. Thermal destressing: Implications for short-circuiting in enhanced geothermal systems. Renewable Energy, 202:736–755, 2023. `doi:10.1016/j.renene.2022.11.102`.
22. David S Mebane, Joel D Kress, Curtis B Storlie, Daniel J Fauth, McMahan L Gray, and Kuijun Li. Transport, zwitterions, and the role of water for co2 adsorption in mesoporous silica-supported amine sorbents. The Journal of Physical Chemistry C, 117(50):26617–26627, 2013. `doi:10.1021/jp4076417`.
23. Aleksandra B Nastasović, Bojana M Ekmešc□ić, Zvjezdana P Sandić, Danijela V Ran□elović, Miran Mozetic□, Alenka Vesel, and Antonije E Onjia. Mechanism of cu (ii), cd (ii) and pb (ii) ions sorption from aqueous solutions

by macroporous poly (glycidyl methacrylate-co-ethylene glycol dimethacrylate). Applied Surface Science, 385:605–615, 2016. `doi:10.1016/j.apsusc.2016.05.165`.

24. Jack Hunter Norbeck and Timothy Latimer. Commercial-scale demonstration of a first-of-a-kind enhanced geothermal system. 2023.
25. SN Pandey, Vikram Vishal, and A Chaudhuri. Geothermal reservoir modeling in a coupled thermo-hydro-mechanical-chemical approach: A review. Earth-Science Reviews, 185:1157–1169, 2018. `doi:10.1016/j.earscirev.2018.09.004`.
26. Roger Parker. The rosemanowes hdr project 1983–1991. Geothermics, 28(4-5):603–615, 1999. `doi:10.1016/S0375-6505(99)00031-0`.
27. Ahinoam Pollack and Tapan Mukerji. Accounting for subsurface uncertainty in enhanced geothermal systems to make more robust techno-economic decisions. Applied energy, 254:113666, 2019. `doi:10.1016/j.apenergy.2019.113666`.
28. M Rahimi, A Shams Khorrami, and P Rezai. Effect of device geometry on droplet size in co-axial flow-focusing microfluidic droplet generation devices. Colloids and surfaces A: physicochemical and engineering aspects, 570:510–517, 2019. `doi:10.1016/j.colsurfa.2019.03.067`.
29. Nicolás Rangel-Jurado, Adam J Hawkins, and Patrick M Fulton. Influence of extreme fracture flow channels on the thermal performance of open-loop geothermal systems at commercial scale. Geothermal Energy, 11(1):19, 2023. `doi:10.1186/s40517-023-00261-7`.
30. Qiang Ren, Haijin Xu, Qiang Yu, and Shiping Zhu. Development of epoxy foaming with co2 as latent blowing agent and principle in selection of amine curing agent. Industrial & Engineering Chemistry Research, 54(44):11056–11064, 2015. `doi:10.1021/acs.iecr.5b03069`.
31. Ridha Ben Said, Joel Motaka Kolle, Khaled Essalah, Bahoueddine Tangour, and Abdelhamid Sayari. A unified approach to co2–amine reaction mechanisms. ACS omega, 5(40):26125–26133, 2020. `doi:10.1021/acsomega.0c03727`.
32. Ashok S Sangani and C Yao. Transport processes in random arrays of cylinders. ii. viscous flow. The Physics of fluids, 31(9):2435–2444, 1988. `doi:10.1063/1.866596`.
33. Tasnuva Sharmin, Nazia Rodoshi Khan, Md Saleh Akram, and M Monjurul Ehsan. A state-of-the-art review on geothermal energy extraction, utilization, and improvement strategies: conventional, hybridized, and enhanced geothermal systems. International Journal of Thermofluids, 18:100323, 2023. `doi:10.1016/j.ijft.2023.100323`.
34. Robert W Zimmerman and Gudmundur S Bodvarsson. Hydraulic conductivity of rock fractures. Transport in porous media, 23:1–30, 1996. `doi:10.1007/BF00145263`.